Cd-based II-VI semiconductor nanostructures produced by buffer-layer-assisted growth: Structural evolution and photoluminescence

P. Swaminathan,[1,3] V. N. Antonov,[2,3] J. A. N. T. Soares,[3] J. S. Palmer,[1,3] and J. H. Weaver[1,2,3]
[1]*Department of Materials Science and Engineering, University of Illinois at Urbana-Champaign, Urbana, Illinois 61801, USA*
[2]*Department of Physics, University of Illinois at Urbana-Champaign, Urbana, Illinois 61801, USA*
[3]*Frederick Seitz Materials Research Laboratory, University of Illinois at Urbana-Champaign, Urbana, Illinois 61801, USA*
(Received 23 December 2005; published 27 March 2006)

II-VI semiconductor nanostructures exhibit interesting optical properties due to quantum confinement of their charge carriers. Here, we discuss the assembly of nanostructures of CdS, CdSe, and CdTe using buffer-layer-assisted growth with Xe buffers. Both compact clusters and ramified wires can be synthesized by varying the Xe buffer layer thickness. Analysis of the nanostructure size distributions and densities makes it possible to calculate their diffusion parameters on the desorbing Xe. Clear differences in the effective activation energies for diffusion for CdS, CdSe, and CdTe can be attributed to differences in London dispersion interactions. Photoluminescence measurements indicate changes from 3D to 2D confinement as compact particles are replaced by ramified wires. Laser power dependent measurements yield the low temperature exciton lifetime, and temperature dependent measurements indicate that optical phonons play a dominant role in the decay of the signal above 50 K and defect states play a dominant role below 50 K.

DOI: 10.1103/PhysRevB.73.125430 PACS number(s): 73.22.−f, 73.61.Ga, 78.55.−m, 68.65.−k

I. INTRODUCTION

II-VI semiconductor nanostructures form an important class of optically active materials due to the size dependence of their exciton energy.[1] There is rich literature that describes synthesis by colloidal routes[2] which yields spherical particles with narrow size distributions.[3] It is also possible to produce rods[4] and tetrapods[5] as well as spherical[6] and branched[7] core-shell structures. Improvements in the functionality of these structures have included doping with transition metal elements, notably Mn (Ref. 8) for potential spintronic applications. They have been used for a wide variety of applications, including quantum light emitting diodes (QLEDs) pigments, and biological tagging.[9] Gur *et al.*[10] recently demonstrated a solar cell with an efficiency of 3% for CdTe-CdSe nanowires spin-coated on indium tin oxide.

While colloidal synthesis offers many advantages, there are issues with regard to integration with current device technology. In particular, solution-based growth is not compatible with the cleanliness essential for fabrication and such growth produces particles that are capped by organic groups that control particle size.[2] Growth by molecular beam epitaxy[11,12] can overcome some of these difficulties, but this requires specific combinations of materials and substrates to give the desired lattice mismatch. Moreover, physical vapor deposition does not yield the size and shape uniformity obtained with colloidal growth.

Buffer-layer-assisted growth (BLAG), developed by Weaver and co-workers,[13–15] is a novel technique that affords growth of a material of choice on a substrate of choice with control over particle size and shape. In BLAG, atoms or molecules are vapor deposited onto thin layers of rare or molecular gas solids that have been grown at low temperature on a substrate. The adatoms interact weakly with the buffer and adatom clusters form spontaneously. Subsequent warm-up activates cluster diffusion, aggregation, and coalescence on the subliming buffer layer. Diffusion is controlled by viscous friction between the cluster and the buffer,[16] and cluster mobility is associated with phononic excitations of the buffer.[17] The average size of the nanostructures delivered on the substrate can be varied over two orders of magnitude by a suitable choice of buffer layer thickness.[13]

Recently, we have shown that it is possible to produce nanostructures of CdSe using BLAG and obtained photoluminescence (PL) signal from them.[18] In this paper, we use Xe buffer layers to form various Cd-based II-VI semiconductor nanostructures. Both compact particles and ramified structures have been synthesized, and their effective diffusion parameters determined. Differences in the activation energies controlling cluster diffusion have been explained based on the nature of the interactions between the nanostructures and Xe. Low temperature PL measurements show the change from 3D to 2D carrier confinement. Power-dependent PL measurements enable us to estimate carrier lifetime at low temperatures and indicate that the main decay mechanism is due to carrier trapping at dangling bond states. Temperature-dependent measurements show that optical phonons play a dominant role in the decay of the PL signal above 50 K and defect states are important below 50 K. BLAG offers a promising way of growing II-VI semiconductors of controlled size and shape directly on various substrates with properties similar to those obtainable by colloidal routes.

II. EXPERIMENTAL DETAILS

Nanoparticles of CdX (X=S,Se,Te) were assembled using BLAG on *n*-doped GaAs (100) wafers on which a 5 nm overlayer of ZnS had been grown at room temperature. GaAs was chosen for ease of optimizing the PL signal using its direct band gap. Simultaneous growth on amorphous carbon grids for TEM (transmission electron microscopy) made it

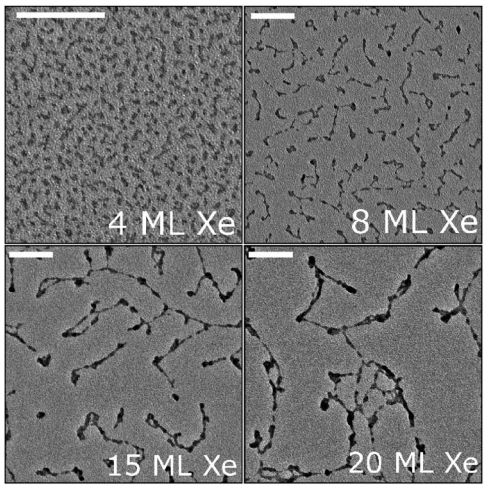

FIG. 1. TEM images of clusters formed by depositing 2 Å CdTe on Xe of 4–20 ML. For thin buffers, the structures are compact. Ramified islands are produced with thicker buffers. They show increasing branch lengths and widths of ~2 nm. The scale bar is 80 nm in each image.

possible to measure particle size distributions and densities. The clusters were grown in a vacuum chamber with a base pressure of $\sim 1 \times 10^{-10}$ Torr. The substrates were cooled to ~20 K using a closed cycle helium refrigerator, and the buffers were grown by condensation with a Xe partial pressure of 1×10^{-6} Torr. The II-VI materials were deposited on the buffer by simple physical vapor deposition. The amount deposited was 1 Å and 2 Å as measured with a quartz crystal oscillator, and the thickness of the buffer was varied from 2 to 20 ML (monolayer). PL measurements were carried out for CdSe and CdTe particles that were capped with a 20 nm layer of ZnS. The ZnS encapsulant confined the photoexcited carriers and passivated surface dangling bonds.

The samples were imaged using a Philips CM 12 TEM. Thousands of clusters from each sample were analyzed to obtain reliable statistics on particle size distributions and densities. High resolution transmission electron microscopy (HRTEM) was performed with a JEOL 2010 LaB_6 to determine the crystal structure and grain size of the particles. The PL measurements used the 458 nm blue line of an Ar ion laser. The detector limited the upper energy to 2.64 eV. The large band gap of bulk CdS (2.48 eV at room temperature) precluded PL studies with this laser. Nominal temperatures of 1.7 K were obtained by pumping on the liquid helium, but laser irradiation raised the sample temperature to 3.9 K. The nominal laser power density was 50 W cm^{-2}. Temperature- and power-dependent PL measurements were also done (3.9–200 K, 5–50 W cm^{-2}).

III. RESULTS AND DISCUSSION

A. Particle growth and morphology

Figure 1 shows the structures formed when 2 Å of CdTe was deposited onto Xe buffers of 4–20 ML in thickness. Analogous images were obtained for CdS and CdSe, with differences described below. The density for the 4 ML Xe buffer corresponds to the initial nucleation density. It reflects the diffusivity of individual molecules on Xe(111) as well as the deposition rate and amount of material deposited.[16] A typical as-nucleated cluster contains ~250 CdTe molecules, and the mean inter-cluster separation is ~10 nm. The initial densities for Cd*X* were $9-11 \times 10^{11}$ cm^{-2}, which are the same, to within experimental error, as those for Ag, Au, and other metal clusters formed on Xe buffers.[16]

The 4 ML results in Fig. 1 show that mostly compact clusters are formed. The presence of some elongated clusters indicates that surface diffusion of Cd*X* on Cd*X* particles is slow compared to metal atoms on metal particles where branching is evident only for much larger structures. Figure 1 also shows a steady reduction in density and the formation of more ramified features as the buffer thickness is increased and cluster diffusion and aggregation increase. The final morphology is dictated by competition between the rates of particle aggregation (caused by diffusion on the buffer) and coalescence (caused by self-diffusion on the aggregate). The relatively slow self-diffusion of Cd*X* is manifested by extensive elongation and branching with small branch widths of ~2–3 nm. These branch widths correspond to the critical size at which compact entities cross over to ramified features. For comparison, we note that images like that of Fig. 1 for 20 ML for similar depositions of Au show compact clusters with a small percentage of elongated islands. When ramified features are eventually formed for Au, they have branch widths of ~10 nm.

The low temperature free energy of formation, obtained by local density calculations, for the zinc blende structure of CdSe is lower that that of the wurtzite structure by 1.4 meV/atom.[19] Figure 2 reproduces HRTEM images of Cd*X* particles to demonstrate that all three compounds crystallize in the cubic zinc blende structure. In contrast, colloidal synthesis of all three compounds tends to produce wurtzite particles,[2] and special steps are required to obtain the zinc blende structure.[8,5] By using BLAG, we can then reach a state that is difficult to reach with other growth techniques. Images obtained along the branches show them to be polycrystalline with a characteristic crystallite size of ~4 nm. Figure 2(d) shows a crystallite formed in a ramified island of CdS. It has (111) orientation relative to the beam, and its boundaries with adjacent crystallites of the island can be seen clearly.

We suspect that the extended branches formed at low temperature during cluster aggregation are amorphous rather than crystalline. This is based on considerations of diffusion on crystalline substrates where the motion of objects larger than trimers or tetramers is negligible unless there is significant lattice mismatch.[20] While the condition of a highly incommensurate interface is satisfied for Au and other metals on Xe, the lattice mismatch for CdSe and Xe is only 2.5% (6.05 Å for CdSe vs 6.20 Å for Xe). If the Cd*X* clusters are amorphous, however, extensive diffusion on the buffer is possible. Thus we conclude that crystallization occurs as the Cd*X* clusters warm to room temperature after their delivery to the substrate at ~75 K. We note that BLAG of Ge and Si produces compact and ramified structures that are amorphous at room temperature, reflecting the stiffness of the purely covalent bonds and the larger barrier for structural change.

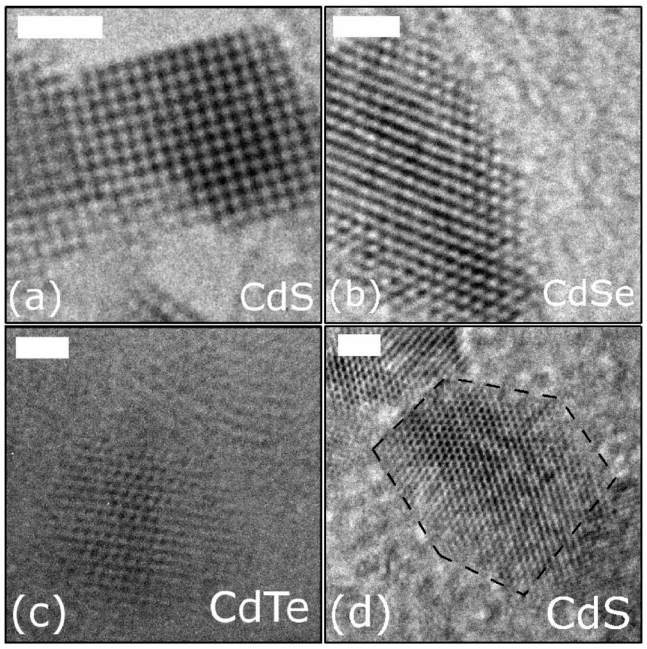

FIG. 2. HRTEM images showing single crystals of (a) CdS, (b) CdSe, and (c) CdTe that exhibit the zinc blende structure. The polycrystalline nature of the aggregated particle in (d) is evident from the presence of planes with different orientations in the same particle. The CdS crystallite enclosed in (d) measures 7 nm in length and 5 nm across the center, and shows a (111) orientation. It was obtained by growing 1 Å CdS on 10 ML Xe. All scale bars are 1 nm in length.

B. Particles diffusivities, activation energies, and their origin

Particle diffusivities in BLAG can be represented by the product of a temperature-independent part, which is inversely proportional to particle/buffer contact area, and an exponentially-dependent temperature part, which is characterized by a size-independent effective activation energy.[16,17] It is important to note that this effective activation energy does not reflect a single potential barrier, as in the case of atomic diffusion, but is a statistical average of the simultaneous interaction of the multiple atoms/molecules at the incommensurate interface between the particle and the buffer.[16]

The Arrhenius parameters for diffusion can be quantified by measuring the particle density as a function of buffer thickness.[16] Figure 3 summarizes the results for Cd*X* where a single particle is counted as unity regardless of whether it is compact or ramified. Diffusion occurs on the buffer during desorption, a process that depends on the buffer thickness, the warm up rate (0.03 K s^{-1}), and the activation energy for buffer species desorption (0.17 eV for Xe). Both Xe desorption and particle diffusion depend exponentially on temperature, which results in a power law relationship between the density and buffer thickness that reflects this competition.[16] Figure 3 reveals that relationship with exponents that vary from −2.44 for CdS to −4.62 for CdSe. Using these exponents, and solving for the time required for a buffer of given thickness to desorb, we can extract the values for the effective activation energy and the prefactor for particle diffusion

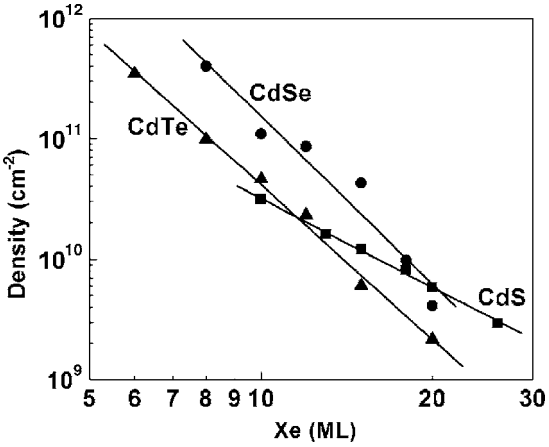

FIG. 3. Particle density vs buffer thickness for 2 Å each of CdS (■), CdSe (•), and CdTe (▲) deposited on the buffer. The lines are best fits to the data. As discussed in the text, the effective activation energies for cluster diffusion on the desorbing Xe buffer can be obtained with the help of these fits.

from the density data, following the procedure developed for BLAG of metal particles in Ref. 17. In particular, the effective activation energy ε_d is determined from the density exponent using

$$\frac{\langle n(\theta_1)\rangle}{\langle n(\theta_2)\rangle} = \left\{ \frac{\int_0^{t(\theta_1)} \exp[-\varepsilon_d/(k\beta t')]dt'}{\int_0^{t(\theta_2)} \exp[-\varepsilon_d/(k\beta t')]dt'} \right\}^{-z}, \qquad (1)$$

where k is the Boltzmann constant, $n(\theta)$ is particle density after desorption of θ monolayers, $t(\theta)$ is the time for this desorption at the warm-up rate β, and $z=z(\rho)$ is the coverage-dependent rate of island density decay, determined from the simulation in Ref. 17. The values of z are −0.65, −0.67, and −0.75 for CdS, CdSe, and CdTe, respectively. The total diffusivities are found by assigning real space and time values to the variables in the simulation, and from these the temperature-independent prefactors are extracted. The values of diffusivity for Cd*X*particles of 100 nm^2 projected area are listed in Table I. It is important to stress that these prefactors do not reflect single atom attempt frequencies, but result from the entropy of multiphonon excitations which

TABLE I. Effective activation energies and prefactors for ramified islands of Cd*X* on the Xe buffer layer as discussed in the text. The prefactors are calculated for an island with a projected area of 100 nm^2.

	Activation energy (eV)	Prefactor (cm^2 s^{-1})
CdS	0.67±0.02	3.68×10^{32}
CdSe	1.09±0.16	3.8×10^{59}
CdTe	1.03±0.04	2.65×10^{56}

TABLE II. Van der Waals interaction parameters between Cd*X* and Xe. U_{dip} represents the permanent dipole moment contribution to the total binding energy. The dipole moment, p, is given by $\pm Zf^{0.5}$. It is given in terms of electron charge and angstroms. Here, f is the Phillips ionicity (Ref. 27) and Z is the bond valence (value=2).

Cd*X*	Bond length (Å)	Phillips ionicity (f)	Dipole moment p (e Å)	Polarizability (per atom) Å^3	U_{dip} (eV)
CdS	2.53	0.685	1.65	3.5	−0.25
CdSe	2.63	0.699	1.67	4.4	−0.26
CdTe	2.81	0.675	1.69	4.7	−0.24

contribute very significantly to the temperature-independent part of the particle diffusivity.[17]

In previous studies of metal nanoparticles, we showed that a plot of the effective activation energy vs the prefactor produces a straight line, the slope of which reflects the reciprocal of the energy of the elementary particles involved in activation—the phonons of Xe. Thus, a higher activation energy means that more buffer phonons are required to supply the corresponding energy. This leads to an increase in the number of ways of assembling those buffer phonons, which introduces entropy that is reflected in the prefactor. Such a behavior, where the prefactor scales exponentially with the activation energy of the process, is called the compensation rule or Meyer-Neldel rule.[21,22] We can test whether diffusion for Cd*X* on Xe follows this behavior by plotting the energies of Table I vs log of the prefactors. Doing so does, in fact, produce an exponential dependence of the prefactor on the energy, and the reciprocal of the slope is 6.7±0.1 meV, in agreement with the value obtained for metal cluster diffusion on Xe.[17] As for metals, we conclude that diffusion of Cd*X* semiconductor particles is related to the Debye energy of solid xenon. A similar analysis for buffers of Kr, Ar, and CO_2 yields values that are related to the elementary excitations of the respective buffers.[23]

The effective activation energies of Table I for Cd*X* cluster diffusion on Xe are significantly higher than those for metals on Xe.[17] In addition, the activation energy for CdS (0.67 eV) is smaller than CdSe (1.09 eV) and CdTe (1.03 eV). These differences reflect the van der Waals interactions between the II-VI semiconductors and the Xe buffer. In particular, the interactions between Cd*X* and Xe arise from two contributions—the permanent dipole of Cd*X* interacting with the induced dipole of Xe and the fluctuating dipole (London dispersion) interaction. Metals do not have a permanent dipole interaction with Xe.

The permanent dipole interaction between Cd*X* and Xe can be estimated from[24]

$$U_{\mathrm{dip}} = -\frac{1}{2}\alpha_{\mathrm{Xe}} p_{\mathrm{Cd}X}^2 \left[\frac{1+3\cos^2\phi}{(4\pi\epsilon_o)^2 r^6}\right], \qquad (2)$$

where α_{Xe} is the polarizability of a Xe atom ($4\pi\varepsilon_o \times 4.044$ Å^3),[25] ϕ is the angle between the Xe atom and the Cd*X* molecular axis, r is the distance between the center of the Cd*X* molecule and Xe, and p_{CdX} is the dipole moment of the molecule. The dipole moments are given by $\pm Zf^{0.5}$,[26] where Z is the valence ($2e$) and f is the Phillips ionicity.[27] These values are included in Table II. Averaging over all possible values of ϕ (the range of 0°–180° corresponds to the extremes where the Xe atom is in line with the Cd*X* molecule and touching either Cd or *X*) and the corresponding values for r yields the permanent dipole contribution to the binding energy, U_{dip}, given in Table II.

The other contribution to the binding energy (and hence the effective activation energy) arises from the London dispersion interaction which depends on the polarizability of the molecule. Values of polarizabilities are given in Table II. For CdSe, the polarizability of 4.4 Å^3 per atom[28] is comparable to that of metals, while the value for CdTe [4.7 Å^3 per atom (Ref. 29)] is slightly higher due to its reduced ionicity. For CdSe and CdTe the dispersion interactions then make similar contributions to the total binding energy and the activation energies are effectively double of those found for metals. Since the polarizability of CdS is lower [3.5 Å^3 per atom (Ref. 30)], we believe that the dispersion interaction contribution is lower and, thus while the activation energy for CdS is still higher than for metals, it is lower than the values for other Cd*X* systems.

C. Low temperature PL and structural origins

PL measurements show how the "band gap" depends on the particle size and how exciton confinement depends on particle shape. Our measurements were carried out at 3.9 K to minimize losses through nonradiative recombination routes. The particles were encapsulated in a ZnS matrix to reduce surface dangling bonds and provide quantum confinement of carriers. Figure 4 shows PL spectra for CdSe and CdTe nanostructures for representative buffer thicknesses, with Fig. 1 giving the corresponding structural information for CdTe clusters. An equivalent evolution was found for the nanostructures of CdSe. The PL spectra track the shape evolution, with differences in coverage and densities. Figure 4(a) shows the PL peak at 2.60 eV for CdSe particles grown by depositing 2 Å on 2 ML Xe, and TEM image analysis shows that the particles are compact with a maximum in the size distribution at ~3 nm. Recent tight binding calculations[31] derived a value of 2.63 eV for the exciton energy for such particles, slightly higher than the observed peak position. Since our particles are capped with ZnS, which provides a finite potential well, quantum confinement effects should be lower due to leakage of wave functions to the ZnS layer. For CdSe particles capped with ZnS, the lowering of peak energy due to the finite potential well is around 0.03–0.06 eV.[32]

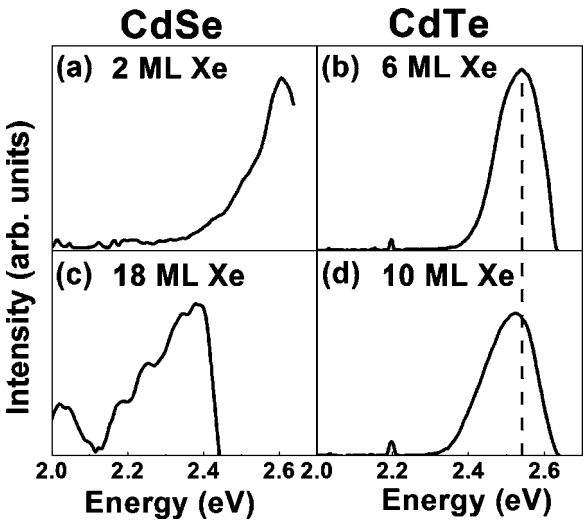

FIG. 4. Low temperature PL spectra for samples of CdSe and CdTe as a function of buffer thickness after background subtraction. The excitation power was 100 mW and the excitation wavelength was 458 nm (2.71 eV). The spectra were recorded at 3.9 K, and the amount of CdSe or CdTe deposited was 2 Å in each case. The high energy cutoff was dictated by the detector. Comparing (a) and (c) for CdSe shows the transition from 3D to 2D quantum confinement since the particles in (a) were compact and those in (c) were highly ramified. The redshift from (b) to (d) reflects the loss of compact particles from the mixed state of particles and rods in (b). The bulk band gaps of CdSe and CdTe are 1.73 and 1.48 eV at room temperature.

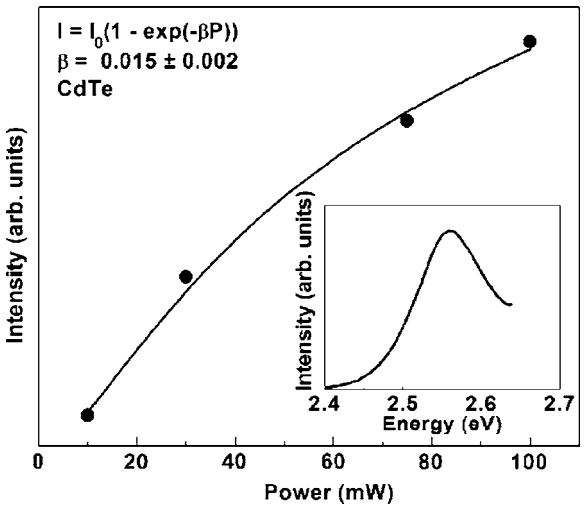

FIG. 5. Integrated PL intensity vs laser power for compact CdTe nanoparticles. The parameter β obtained from the fit can be used to calculate the exciton lifetime at low temperature. The sample was produced by depositing 1 Å CdTe on a 10 ML Xe buffer layer. TEM analysis indicates compact particles with a peak in the size distribution at 3 nm. The inset shows the PL spectrum at 100 mW, with the cut off at 2.64 eV being due to the detector.

Figure 4(b) shows the PL spectrum from a sample obtained by deposition of 2 Å CdTe on 6 ML Xe. In this case, there is a mixture of compact and elongated particles with a continuous size distribution. PL peak seen at 2.55 eV reflects this mixture of rods and dots. A further increase in buffer thickness produces ramified islands where confinement is different along the length and width of the branches. For lengths greater than several times the exciton Bohr radius, confinement is dictated solely by the widths of the branches.[33] In this case, the spectrum of Fig. 4(d) for 2 Å CdTe grown on 10 ML Xe shows two-dimensional confinement in the ramified islands. These islands have widths of ~2 nm and lengths varying over a few tens of nm. The PL spectrum is redshifted with respect to the spectrum from 6 ML Xe, and the peak value of 2.50 eV agrees well with values obtained for CdTe wires by Zhiyong *et al.*[34] (after extrapolating to wires of 2 nm diameter and 4 K). Growth on even thicker buffers produces ramified islands with lengths running into hundreds of nm. For example, the PL spectrum of Fig. 4(c) is from 2 Å CdSe grown on 18 ML Xe where the length is a few hundreds of nm but the width is ~3 nm. The PL peak around 2.4 eV is in good agreement with data obtained on colloid grown wires of similar diameter.[35]

D. Power dependence of PL and exciton lifetimes

Figure 5 shows how the integrated intensity of the PL signal changes with excitation power, and the intensity change can be used to determine the exciton lifetime. The line represents a fit to an exponential function where the exponential dependence arises from the presence of nanocrystals with multiple excitons. The total number of excitons (N) created in a nanocrystal is proportional to the incident laser power P,[36]

$$N = \beta P = \tau_{\mathrm{ex}} \sigma \Gamma = \tau_{\mathrm{ex}} (\mu \mathrm{V}) \left(\frac{P}{A h \nu} \right), \tag{3}$$

where β is the proportionality factor, Γ is the photon flux, σ is the absorption cross section given by μV, μ is the absorption coefficient, V is the volume of the nanoparticle, A is the laser beam cross section, $h\nu$ is the excitation energy, and τ_{ex} is the exciton lifetime. If we have n nanocrystals, the distribution of the N excitons among them can be estimated from the Poisson distribution[37] arising from the random distribution of excitons among the nanocrystals. At low excitation intensities, the number of nanocrystals with just one exciton is $n_o = n[1 - \exp(-\beta P)]$.[37] Thus, the intensity of the signal (proportional to the number of nanocrystals with a single exciton) is exponentially dependent on the laser power P with $\beta = 0.015 \pm 0.002$ mW^{-1} obtained from the fit in Fig. 5. With $h\nu = 2.712$ eV, $\mu = 3.52 \times 10^4$ cm^{-1} for that energy[38] and considering particles of diameter 3 nm (peak in the size distribution), we obtain $\tau_{\mathrm{ex}} = 25 \pm 4$ ns for CdTe nanoparticles. We expect a similar value lifetime of CdSe particles as well. In comparison, colloidal CdSe quantum dots exhibit a radiative lifetime of the order of a few hundred ns at 4 K.[39] The low value observed here indicates the presence of defect states that act as nonradiative decay channels for the excitons

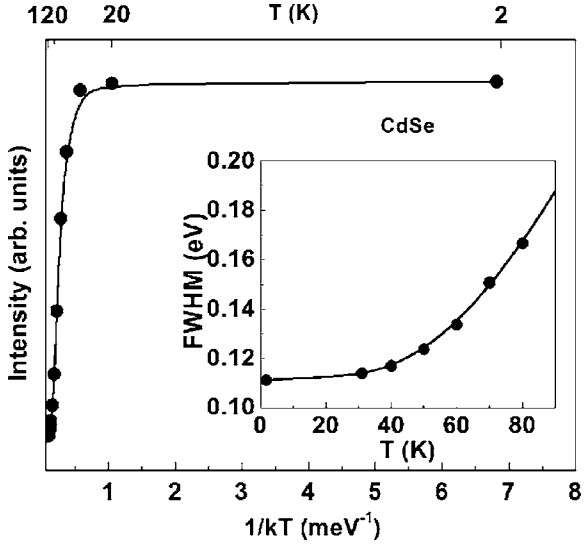

FIG. 6. Temperature dependence of the peak intensity shown as a semilog plot of the integrated intensity vs the inverse temperature. The inset shows the full width at half maximum (FWHM) of the peak. These results can be used to extract the LO phonon-electron coupling coefficient and energy and also rates of phonon- and defect-assisted decay. The sample is 1 Å CdSe on 6 ML Xe (compact particles with ~4 nm diameter).

and arise from the incomplete passivation by room temperature overgrowth of ZnS.

E. Temperature dependence of PL and electron-phonon interactions

Temperature dependent PL measurements provide information related to electron-phonon interactions. These measurements were carried out with 1 Å CdSe grown on 6 ML Xe which resulted in compact particles with a maximum in the size distribution at ~3 nm. Figure 6 shows that the intensity remains almost a constant up to ~20 K, with an exponential decrease at high temperature. The inset of the figure shows the increase in peak width with temperature, which can be used to obtain the exciton-phonon coupling relation in the CdSe dots. This is done by fitting the full width at half maximum (FWHM) dependence with a linear *plus* reciprocal exponential function of temperature[40]

$$\mathrm{FWHM} = W_{\mathrm{Inh}} + \alpha T + W_{\mathrm{LO}}\left[\exp\left(\frac{E_{\mathrm{LO}}}{kT}\right) - 1\right]^{-1}, \quad (4)$$

where W_{Inh} represents inhomogeneous broadening determined by the size distribution, α represents the exciton-acoustic phonon coupling, E_{LO} represents the exciton-optical phonon coupling energy, and W_{LO} is its prefactor. The value of $\alpha = 60 \pm 5$ μeV/K obtained from the fit is close to the theoretical value of 50 μeV/K obtained for 3 nm diameter particles of CdSe,[41] and it is much higher than for bulk CdSe (8 μeV/K). The higher value of the acoustic phonon coupling for nanoparticles compared to the bulk value has been explained in terms of the increased deformation potential and polarization coupling.[42] The exciton-optical phonon coupling energy is given by the exponential portion of the fit, and its value is $E_{\mathrm{LO}} = 18 \pm 2$ meV. A value lower than the bulk optical phonon energy is expected for nanocrystals, and our value agrees well with those calculated for particles of 3 nm diameter.[43]

The integrated intensity of the PL peak as a function of temperature can be used to obtain the main exciton decay mechanism. Signal decay can occur due to trapping of excitons in defect states and also due to coupling with phonons of the nanocrystals. The relative importance of the two processes can be obtained by fitting the intensity of the PL signal to two decay modes[43]

$$I(T) = I_O\left[1 + R_a \exp\left(-\frac{E_a}{kT}\right) + R_{\mathrm{ph}}\left\{\exp\left(\frac{E_{\mathrm{LO}}}{kT}\right) - 1\right\}^{-n}\right]^{-1}, \quad (5)$$

where the first exponential term represents the rate for carrier trapping at defects (with prefactor R_a and activation energy E_a) and the second represents the decay rate due to phonons, with prefactor R_{ph}. E_{LO} was obtained from the FWHM fit, and the value of n indicates the number of optical phonons that are involved in the transition. A fit to Eq. (5) yields $R_a = 5 \pm 3$, $E_a = 8.7 \pm 1.5$ meV, $R_{\mathrm{ph}} = 460 \pm 137$, and $n = 1.4 \pm 0.1$. At low temperature, the main decay mechanism is defect trapping, with phonon assisted decay playing a major role above 50 K. The low value for the activation energy for defect trapping (8.7 meV) indicates that trapping at surface states is the main decay channel at low temperatures and is consistent with the low exciton lifetimes found in power-dependent measurements at liquid helium temperatures. Future experiments will focus on effects of annealing and high temperature growth of the ZnS-Cd*X* interface on the PL signal.

IV. SUMMARY

We have shown that nanostructures of II-VI compound semiconductors can be grown on a substrate of choice by BLAG with considerable control over the particle size and shape. Regarding the interactions during BLAG growth, significantly higher effective activation energies for diffusion are deduced, compared to metal particle aggregation, and this is attributed to a greater binding energy between the particles and the xenon substrate. It arises from a permanent-dipole-induced interaction that adds on to the London dispersion interaction. The effective activation energy for CdS is lower than CdSe and CdTe because of its lower polarizability and the lower dispersion forces. An understanding of II-VI semiconductor growth by BLAG can be used to generalize growth of other compounds. For example, growth of ionic materials on Xe would depend mainly on their dipole moment. Similarly, growth on other molecular buffers, like amorphous solid water or crystalline ice, would need to take into account the permanent dipole moment of water and its interaction with the growing clusters. These factors would be important in predicting nanostructure morphology for various cluster/buffer systems in the design of novel nanostructures.

Strong PL signals were obtained from the particles at low temperature. PL measurements track the particle morphologies from compact dots to mixtures of dots and particles and rods and then ramified islands of a few hundred nanometers in length. Temperature- and power-dependent measurements shed light on the quality of the interface between the particles and their encapsulating ZnS matrix. Temperature-dependent measurements indicate that the main decay mechanism involves optical phonons above 50 K. Defect states play an important role in signal decay at low temperatures only (below 50 K). Power dependent measurements indicate that the carrier lifetimes are lower than those in colloidal particles because of the low activation energy for trapping at defects. These defects are associated with dangling bonds on the surface due to incomplete passivation. Improvements in signal can be obtained by annealing the samples or growing the capping and base layers at higher temperatures. Quantum dots grown by BLAG should be suitable for integration with existing device technology because dots can be deposited under ultra high vacuum conditions on any substrate, and they offer promise for design of new and improved devices.

ACKNOWLEDGMENTS

This work was supported by the U.S. Department of Energy Division of Materials Sciences under Grant No. DEFG02-01ER45944. The TEM imaging was done in the Center for Microanalysis of Materials, and the photoluminescence measurements were done in the Laser and Spectroscopy Facility of the Frederick Seitz Materials Research Laboratory, which is partially supported by the U.S. Department of Energy under Grant No. DEFG02-91ER45439. We thank A. S. Bhatti and S. G. Bishop for stimulating discussions.

[1] A. P. Alivisatos, Science **271**, 933 (1996).
[2] C. B. Murray, C. R. Kagan, and M. G. Bawendi, Annu. Rev. Mater. Sci. **30**, 545 (2000).
[3] Xiaogang Peng, J. Wickham, and A. P. Alivisatos, J. Am. Chem. Soc. **120**, 5343 (1998).
[4] Xiogang Peng, Liberato Manna, Weidong Yang, Juanita Wickham, Erik Scher, Andreas Kadavanich, and A. P. Alivisatos, Nature (London) **404**, 59 (2000).
[5] Liberato Manna, Delia J. Milliron, Andreas Meisel, Erik C. Scher, and A. P. Alivisatos, Nat. Mater. **2**, 382 (2003).
[6] Xiaogang Peng, Michael C. Schlamp, Andreas V. Kadavanich, and A. P. Alivisatos, J. Am. Chem. Soc. **119**, 7019 (1997).
[7] Delia J. Milliron, Steven M. Hughes, Yi Cui, Liberato Manna, Jingbo Li, Lin-Wang Wang, and A. P. Alivisatos, Nature (London) **430**, 190 (2004).
[8] Steven C. Erwin, Lijun Zu, Michael I. Haftel, Alexander L. Efros, Thomas A. Kennedy, and David J. Norris, Nature (London) **436**, 91 (2005).
[9] X. Michalet, F. F. Pinaud, L. A. Bentolila, J. M. Tsay, S. Doose, J. J. Li, G. Sundaresan, A. M. Wu, S. S. Gambhir, and S. Weiss, Science **307**, 538 (2005).
[10] Ilan Gur, Neil A. Fromer, Michael L. Geier, and A. P. Alivisatos, Science **310**, 462 (2005).
[11] G. Karczewski, S. Mackowski, M. Kutrowski, T. Wojtowicz, and J. Kossut, Appl. Phys. Lett. **74**, 3011 (1999).
[12] S. Mackowski, G. Prechtl, W. Heiss, F. V. Kyrychenko, G. Karczewski, and J. Kossut, Phys. Rev. B **69**, 205325 (2004).
[13] L. Huang, S. J. Chey, and J. H. Weaver, Phys. Rev. Lett. **80**, 4095 (1998).
[14] G. D. Waddill, I. M. Vitomirov, C. M. Aldao, and J. H. Weaver, Phys. Rev. Lett. **62**, 1568 (1989).
[15] J. H. Weaver and G. D. Waddill, Science **251**, 1444 (1991).
[16] V. N. Antonov, J. S. Palmer, A. S. Bhatti, and J. H. Weaver, Phys. Rev. B **68**, 205418 (2003).
[17] V. N. Antonov, J. S. Palmer, P. S. Waggoner, A. S. Bhatti, and J. H. Weaver, Phys. Rev. B **70**, 045406 (2004).
[18] V. N. Antonov, P. Swaminathan, J. A. N. T. Soares, J. S. Palmer, and J. H. Weaver, Appl. Phys. Lett. **88**, 121906 (2006).
[19] Chin-Yu Yeh, Z. W. Lu, S. Froyen, and Alex Zunger, Phys. Rev. B **46**, 10086 (1992).
[20] P. Deltour, J. L. Barrat, and P. Jensen, Phys. Rev. Lett. **78**, 4597 (1997).
[21] W. Meyer and H. Neldel, Z. Tech. Phys. (Leipzig) **12**, 588 (1937).
[22] A. Yelon, B. Movaghar, and H. M. Branz, Phys. Rev. B **46**, 12244 (1992).
[23] P. S. Waggoner, J. S. Palmer, V. N. Antonov, and J. H. Weaver, Surf. Sci. **596**, 12 (2005).
[24] Bo E. Sernelius, *Surface Modes in Physics* (Wiley-VCH, Berlin, 2001).
[25] J. K. Nagle, J. Am. Chem. Soc. **112**, 4741 (1990).
[26] S. H. Wemple, Phys. Rev. B **7**, 4007 (1973).
[27] J. C. Phillips, Rev. Mod. Phys. **42**, 317 (1970).
[28] Eran Rabani, Balazs Hetenyi, B. J. Berne, and L. E. Brus, J. Chem. Phys. **110**, 5355 (1999).
[29] V. Kumar, G. M. Prasad, and D. Chandra, J. Phys. Chem. Solids **58**, 463 (1997).
[30] M. Claudia Troparevsky and J. R. Chelikowsky, J. Chem. Phys. **114**, 943 (2001).
[31] Sameer Sapra and D. D. Sarma, Phys. Rev. B **69**, 125304 (2004).
[32] B. O. Dabbousi, J. Rodriguez-Viejo, F. V. Mikulec, J. R. Heine, H. Mattoussi, R. Ober, K. F. Jensen, and M. G. Bawendi, J. Phys. Chem. B **101**, 9463 (1997).
[33] S. V. Gaponenko, *Optical Properties of Semiconductor Nanocrystals* (Cambridge University Press, Cambridge, 1998).
[34] Zhiyong Tang, Nicholas A. Kotov, and Michael Giersig, Science **297**, 237 (2002).
[35] L.-s. Li, J. Hu, W. Yang, and A. P Alivisatos, Nano Lett. **1**, 349 (2001).
[36] V. Babentsov, J. Riegler, J. Schneider, M. Fiederle, and T. Nann, J. Phys. Chem. B **109**, 15349 (2005).
[37] J. Michel Caruge, Y. Chan, V. Sundar, H. J. Eisler, and M. G. Bawendi, Phys. Rev. B **70**, 085316 (2004).

[38] A. E. Rakshani, J. Appl. Phys. **81**, 7988 (1997).
[39] S. A. Crooker, T. Barrick, J. A. Hollingsworth, and V. I. Klimov, Appl. Phys. Lett. **82**, 2793 (2003).
[40] Johnson Lee, Emil S. Koteles, and M. O. Vassell, Phys. Rev. B **33**, 5512 (1986).
[41] T. Takagahara, J. Lumin. **70**, 129 (1996).
[42] C. Trallero-Giner, A. Debernardi, M. Cardona, E. Menendez-Proupin, and A. I. Ekimov, Phys. Rev. B **57**, 4664 (1998).
[43] D. Valerini, A. Creti, M. Lomascolo, L. Manna, R. Cingolani, and M. Anni, Phys. Rev. B **71**, 235409 (2005).